



**HAL**  
open science

# Simulated mass measurements of the young planet K2-33b

Baptiste Klein, J-F Donati

► **To cite this version:**

Baptiste Klein, J-F Donati. Simulated mass measurements of the young planet K2-33b. *Monthly Notices of the Royal Astronomical Society: Letters*, 2020, 493 (1), pp.L92-L97. 10.1093/mnrasl/slaa009 . hal-03008481

**HAL Id: hal-03008481**

**<https://cnrs.hal.science/hal-03008481>**

Submitted on 7 Jul 2023

**HAL** is a multi-disciplinary open access archive for the deposit and dissemination of scientific research documents, whether they are published or not. The documents may come from teaching and research institutions in France or abroad, or from public or private research centers.

L'archive ouverte pluridisciplinaire **HAL**, est destinée au dépôt et à la diffusion de documents scientifiques de niveau recherche, publiés ou non, émanant des établissements d'enseignement et de recherche français ou étrangers, des laboratoires publics ou privés.

# Simulated mass measurements of the young planet K2-33b

Baptiste Klein<sup>1,2★</sup> and J.-F. Donati<sup>1,2</sup>

<sup>1</sup>Universite de Toulouse, UPS-OMP, IRAP, 14 Avenue E. Belin, Toulouse F-31400, France

<sup>2</sup>CNRS, IRAP/UMR 5277, Toulouse, 14 Avenue E. Belin, Toulouse F-31400, France

Accepted 2020 January 12. Received 2020 January 10; in original form 2019 October 15

## ABSTRACT

In this paper, we carry out simulations of radial velocity (RV) measurements of the mass of the 8–11 Myr Neptune-sized planet K2-33b using high-precision near-infrared velocimeters like SPIRou at the Canada–France–Hawaii Telescope. We generate an RV curve containing a planet signature and a realistic stellar activity signal, computed for a central wavelength of 1.8  $\mu\text{m}$  and statistically compatible with the light curve obtained with K2. The modelled activity signal includes the effect of time-evolving dark and bright surface features hosting a 2 kG radial magnetic field, resulting in an RV signal of semi-amplitude  $\sim 30 \text{ m s}^{-1}$ . Assuming a 3-month visibility window, we build RV time series including Gaussian white noise from which we retrieve the planet mass while filtering the stellar activity signal using Gaussian process regression. We find that 35/50 visits spread over three consecutive bright-time runs on K2-33 allow one to reliably detect planet RV signatures of, respectively, 10 and 5  $\text{m s}^{-1}$  at precisions  $> 3\sigma$ . We also show that 30 visits may end up being insufficient in some cases to provide a good coverage of the stellar rotation cycle, with the result that the planet signature can go undetected or the mass estimation be plagued by large errors.

**Key words:** methods: statistical – techniques: radial velocities – stars: activity – stars: individual: K2-33 – planetary systems.

## 1 INTRODUCTION

Planet formation and evolution models critically need observational constraints on how planet bulk densities vary with time in the early stages of their lives (e.g. Mordasini et al. 2012; Alibert et al. 2013). This requires to measure radii of transiting planets through the relative depths of their photometric transits on the one hand, and masses through the semi-amplitudes of their radial velocity (RV) curves, on the other hand. Both measurements are challenging for pre-main-sequence (PMS) stars known to exhibit intense magnetic activity (e.g. Bouvier & Bertout 1989) inducing photometric and RV fluctuations that largely overshadow the planet signatures (e.g. Crockett et al. 2012). As a result, only a handful of candidate close-in giant planets younger than 20 Myr have been unveiled so far, either using RV observations (Donati et al. 2016; Johns-Krull et al. 2016; Yu et al. 2017) or transit photometry (David et al. 2016; Mann et al. 2016; David et al. 2019a,b). None of them have a well-measured bulk density.

Observing PMS stars in the near-infrared (nIR) rather than in the V band should make it easier to separate the planet signature from the stellar activity signal as the latter is expected to be weaker in this domain (Mahmud et al. 2011) and the stars are significantly reddened. High-precision nIR velocimeters like SPIRou (Donati

et al. 2018), CARMENES (Quirrenbach et al. 2014), GIARPS (Claudi et al. 2017), or NIRPS (Wildi et al. 2017) are thus the most promising instruments worldwide to carry out mass measurements of close-in transiting planets orbiting PMS stars. Magnetic fields are however expected to affect stellar RV activity signals (Reiners et al. 2013; Hébrard et al. 2014), making the problem non-trivial and worth a detailed simulation study. This is especially relevant given that 300 nights of Canada-France-Hawaii Telescope (CFHT) time are already allocated to the SPIRou Legacy Survey (SLS), some of them being dedicated to the RV follow-up of stars hosting transiting planets, with the goal of measuring the planet masses.

K2-33 is an 8–11 Myr M3 PMS star located in Upper Scorpius that was shown to host a 5- $R_{\oplus}$  close-in transiting planet (David et al. 2016; Mann et al. 2016, hereafter D16 and M16, respectively) from the 80-d continuous light curve obtained during campaign 2 of the K2 mission (Howell et al. 2014). K2-33 will be observed with SPIRou as part of the SLS in an attempt to measure the mass of its close-in planet through RV observations. In this study, we propose to use K2-33 as a representative of the PMS stars to be observed within the SLS. We simulate SPIRou RV observations of this star and attempt retrieving the RV signature of the Neptune-sized planet assuming various planet masses, sampling schemes and levels of white noise. In Section 2, we outline how we generate the realistic synthetic time series for K2-33 and, in Section 3, their modelling in order to filter the stellar activity signal while estimating the

\* E-mail: [baptiste.klein@irap.omp.eu](mailto:baptiste.klein@irap.omp.eu)

**Table 1.** Main stellar properties used to generate stellar activity photometric and RV curves for K2-33.

Parameter	Value	Notes
$P_{\text{rot}}$	6.35 d	Main peak in ACF (see Fig. 2)
$v \sin i$	$8.2 \text{ km s}^{-1}$	From M16
$T_{\text{eff}}$	3475 K	Average between M16 and D16
$i$	$88^\circ$	Average between M16 and D16
$p_r$	0.3 per cent	–
$\log_{10} s_r$	$\mathcal{N}(-2.6, 0.1)$	–
$t_r$	$18.0 P_{\text{rot}}$	Rescaled by a factor $\propto s_r$

planet parameters. We finally summarize our results and discuss their implications in Section 4.

## 2 SYNTHETIC RV DATA SETS

Our method to simulate RV observations of K2-33 with SPIRou is similar to that described in Klein & Donati (2019, hereafter K19). We first generate a densely sampled RV curve, containing a planet signature and a stellar activity signal whose statistical properties are consistent with that of the K2 light curve which encloses information about the evolution properties of the features at the surface of the star. We then create RV time series by selecting observation dates using different schemes and adding noise to account for the various sources that may affect the data.

### 2.1 Stellar activity RV curve

Using the method described in K19, we model the stellar surface into a dense grid of 100 000 cells and generate 80 d densely sampled photometric and RV curves. This model includes time-evolving bright/dark features whose effective temperatures are scaled from Berdyugina (2005) and whose brightnesses are inferred using Planck’s law at K2 and SPIRou central wavelengths, respectively, for the photometric and RV curves. Each feature is also assumed to host a radial magnetic field of 2 kG to account for the significant Zeeman splitting of the line profiles at SPIRou’s central wavelength (e.g. Reiners et al. 2013).

We tune the appearance probability  $p_r$  of activity features at the surface of the star at each time-step as well as their lifetimes  $t_r$  and maximum relative areas  $s_r$  so as the autocorrelation function (ACF) of the synthetic photometric curve is similar to that of the K2 light curve detrended with the EVEREST software (Luger et al. 2016, 2018). The stellar parameters adopted to generate the stellar activity curves are shown in Table 1. Note that we rescaled the total lifetime of each injected feature by a factor  $\propto s_r$  so that the larger the feature, the longer its lifetime, in agreement with what is observed on the K2 light curve. The photometry and RV curves resulting from our activity model are shown in Fig. 1. Their ACFs are superimposed to that of the detrended K2 light curve in Fig. 2, showing a good overall agreement.

We then compare the statistical properties of the newly synthesized photometric and RV curves to that of the K2 light curve by independently modelling the rotationally modulated component within each curve using Gaussian process regression (GPR; Rasmussen & Williams 2006). The K2 light curve being affected by short-lived phenomena like flares and planetary transits, we use a specific process to extract the signal produced by inhomogeneities at the surface of the star. We first build a reduced photometric data set by dividing the K2 light curve into 200 consecutive time intervals

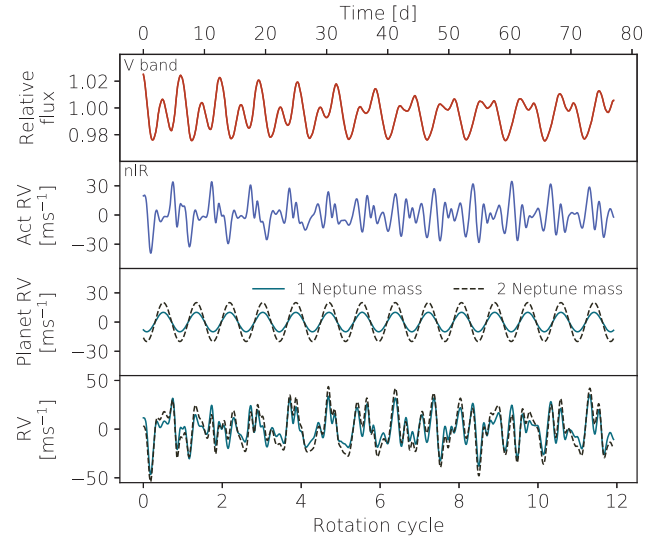


**Figure 1.** Synthetic photometry and RV curves of K2-33. From top to bottom: synthetic relative brightness curve in K2 spectral band; corresponding stellar activity RV curve at SPIRou’s central wavelength; expected planet RV signatures for semi-amplitudes of 10 and 20  $\text{m s}^{-1}$  (blue solid line and black dashed line, respectively); resulting RV curves.

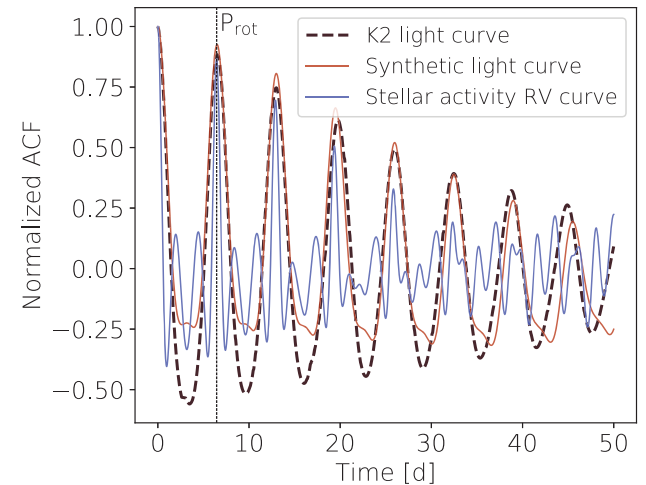


**Figure 2.** ACFs of the EVEREST-detrended K2 light curve (black dashed line), synthetic photometric curve (red solid line), and synthetic stellar activity RV curve (blue solid line). The stellar rotation period is indicated by the vertical dashed line.

of equal duration and then by computing the median of all the points within each interval. We then model the resulting 200-point light curve using GPR assuming a quasi-periodic covariance kernel (e.g. Haywood et al. 2014),  $k$ , which relies on a vector of four so-called hyperparameters,  $\theta$ , such that

$$k(t_i, t_j) = \theta_1^2 \exp \left[ -\frac{(t_i - t_j)^2}{\theta_2^2} - \frac{\sin^2 \frac{\pi(t_i - t_j)}{\theta_3}}{\theta_4^2} \right], \quad (1)$$

where  $t_i$  and  $t_j$  are the times associated with observations  $i$  and  $j$ , and  $\theta_1$  to  $\theta_4$ , respectively, stand for the amplitude, evolution time-scale, recurrence period, and smoothing factor of the Gaussian Process (GP).  $\theta$  is estimated by maximizing its posterior density sampled using a Bayesian Markov Chain Monte Carlo (MCMC) process. We then use the trained GP to predict the values of the rotationally

**Table 2.** Prior densities ( $\pi$ ; columns 2 and 3), and best estimates of  $\theta$  (columns 4–6) obtained when modelling the stellar activity photometry ( $Y_k$  and  $Y_s$  for K2 and synthetic curves respectively) and RV ( $V_s$ ) curves.  $\mathcal{U}$  stands for the uniform distribution. Note that we use the Gaussian distribution  $\mathcal{N}(6.35d, 0.04d)$  as a prior density law for  $\theta_3$  when modelling the RV time series described in Section 3.

Param.	$\pi(\theta Y_k), \pi(\theta Y_s)$	$\pi(\theta V_s)$	$Y_k$	$Y_s$	$V_s$
$\ln \theta_1$	$\mathcal{U}(-10, 1)$	$\mathcal{U}(-2, 7)$	$-4.6 \pm 0.2$	$-4.9 \pm 0.2$	$2.9 \pm 0.2$ [ $\ln \text{m s}^{-1}$ ]
$\ln(\theta_2[\text{d}])$	$\mathcal{U}(1.0, 7.0)$	$\mathcal{U}(1.0, 7.0)$	$2.94 \pm 0.04$	$3.27 \pm 0.08$	$3.58 \pm 0.10$
$\theta_3$ [d]	$\mathcal{U}(5.5, 7.5)$	$\mathcal{U}(6.25, 6.65)$	$6.35 \pm 0.04$	$6.36 \pm 0.02$	$6.35 \pm 0.01$
$\theta_4$	$\mathcal{U}(0.1, 5.0)$	$\mathcal{U}(0.1, 4.0)$	$1.01 \pm 0.1$	$0.71 \pm 0.06$	$0.33 \pm 0.02$

modulated photometric signal at the times of K2 observations and reject the points deviating from the GPR prediction by more than  $3\sigma$ , then repeat the process until no point is rejected. The prior densities used for the hyperparameters as well as their best estimates are shown in Table 2.

We select 250 evenly sampled data points from the densely sampled synthetic photometric and RV curves, add a Gaussian white noise of respectively  $\sim 300$  ppm and  $2 \text{ m s}^{-1}$  and use GPR to independently model the two data sets (called  $Y_s$  and  $V_s$ , respectively) in order to estimate their statistical properties. The outcome of the fit as well as the adopted prior densities are given in Table 2 (rms of the residuals of 300 ppm and  $1.8 \text{ m s}^{-1}$  for  $Y_s$  and  $V_s$ , respectively). The significantly larger  $\theta_2$  in the RV time series comes from the fact that the RV activity signal is dominated by the larger, slowly evolving features, whereas the signatures of the smaller, rapidly evolving features are partly drowned in the Gaussian white noise. Conversely, we note that  $\theta_4$  is roughly twice as large in photometry than in RV, which is expected given that a feature at the stellar surface produces an RV signature that evolves roughly twice as fast as its photometric counterpart (see Aigrain, Pont & Zucker 2012). We also observe notable variations of  $\theta_2$  and  $\theta_4$  between the two photometric time series ( $Y_k$  and  $Y_s$ ), indicating (i) slightly longer evolution time-scales for the modelled features and (ii) a lower smoothing factor for the synthetic light curve.

## 2.2 Planet RV curve

Consistently with the modelled planet transit curves of M16, we assume that K2-33b's orbit is circular, and thus that the expected RV signal that the planet induces in the spectrum of its host star is given by

$$V_r(t) = K_p \cos\left(\frac{2\pi}{P_{\text{orb}}}t + \phi_p\right), \quad (2)$$

where  $K_p$ ,  $P_{\text{orb}}$  and  $\phi_p$  are respectively the semi-amplitude, orbital period, and phase of the signal. Since the planet mass is the main parameter we aim at characterizing, and as such is not well known, we consider different values for  $K_p$  listed along with the corresponding planet mass (computed using the parameters reported in D16 or M16) in Table 3. In what follows, we assume that the planet orbital period and phase are given by the average of the values measured by D16 and M16.

## 2.3 Creating the time series

From the densely sampled stellar activity and planet curves described above, we generate RV time series assuming that observations are carried out from the CFHT during three consecutive 15 d-bright time periods centred on full moons. Among the potentially observable nights included in our visibility window, we build data

**Table 3.** Summary of K2-33b parameters reported in D16 and M16 (columns 3 and 4, respectively). The planet masses,  $M_p$ , are computed by means of Kepler's third law using the stellar mass and planet orbital period reported in each article ( $M_{\oplus}$  standing for Neptune mass).

Source		David et al. (2016)	Mann et al. (2016)
$K_p$	$5 \text{ m s}^{-1}$	$M_p = 0.37 M_{\oplus}$	$M_p = 0.54 M_{\oplus}$
	$10 \text{ m s}^{-1}$	$M_p = 0.73 M_{\oplus}$	$M_p = 1.09 M_{\oplus}$
	$20 \text{ m s}^{-1}$	$M_p = 1.47 M_{\oplus}$	$M_p = 2.18 M_{\oplus}$
$P_{\text{orb}}$		5.42513 d	5.424865 d
$\phi_p$		0.374 rad	0.375 rad

sets with  $N = 30, 35, 40$  randomly selected data points at airmass  $\lesssim 1.8$ . We also consider a more optimistic case with data sets of  $N = 50$  data points randomly selected on three consecutive CFHT bright time periods of 20 d each. For each value of  $N$ , we build 8 sets of 10 RV time series with different realizations of white noise, each set being drawn using a different distribution of observing epochs. We deal with the various sources of noise expected to pollute the RV time series (e.g. photon and instrument noises) by adding a centred Gaussian white noise with standard deviations,  $\sigma_n$ , of  $2 \text{ m s}^{-1}$  for an optimistic case, or  $5 \text{ m s}^{-1}$  for a more conservative case achievable for velocimeters like SPIRou on as faint a target as K2-33.

## 3 MODELLING THE TIME SERIES

### 3.1 Method

We model the synthetic RV time series using the method detailed in K19. Assuming that  $P_{\text{orb}}$  is known from photometry, the planet RV signature described by equation (2) can be expressed as a linear function of parameters depending on  $K_m$  and  $\phi_m$ , i.e. respectively the semi-amplitude and orbital phase of the RV signal induced by the planet on the stellar spectrum to recover. The stellar activity RV signal is modelled using GPR assuming the four-parameter quasi-periodic covariance kernel defined in equation (1). We use the EMCEE affine invariant sampler (Foreman-Mackey et al. 2013, 5000 iterations of 100 walkers) to sample the posterior density of the model marginalized over the planet parameters. The prior densities adopted for  $\theta$  are given in Table 2. The median and  $1\sigma$  error bars on  $\theta$  are computed from the posterior densities after removing a burn-in period of  $\sim 100\,000$  steps (i.e. 1000 iterations of 100 walkers), while the planet parameters are estimated using a least-squares estimator computed at the value of  $\theta$  that maximizes the likelihood of the model (hereafter  $\theta_b$ ). The resulting Gaussian posterior density for  $K_m$  is convolved with the distribution of the semi-amplitudes of the planetary signal obtained by applying the aforementioned least-squares estimator to  $\sim 50\,000$  samples  $\theta$  (i.e. 500 iterations of 100 walkers), in order to account for correlations

**Table 4.** Results of the fit to RV time series for various  $N$  and  $K_p$  at  $\sigma_n = 2 \text{ m s}^{-1}$ .  $\tau_c$  and  $\tau_b$  stand for the fractions of data sets rejected due to an unrealistic  $\theta_b$  and a too low value for  $B_F$ , respectively. The values shown in each line are averaged over all the remaining RV data sets of given  $N$  and  $K_p$ .

$K_p$ ( $\text{m s}^{-1}$ )	$N_{\text{pts}}$	$\tau_c$ (per cent)	$\tau_b$ (per cent)	$\ln \theta_1$ ( $\ln \text{m s}^{-1}$ )	$\ln \theta_2$ ( $\ln \text{d}$ )	$\theta_3$ ( $\text{d}$ )	$\theta_4$	$K_m$ ( $\text{m s}^{-1}$ )	rms ( $\text{m s}^{-1}$ )	$\ln \mathcal{L}_{\text{max}}$	$\ln \text{BF}$
5	30	23	1	$2.52 \pm 0.18$	$3.79 \pm 0.70$	$6.37 \pm 0.03$	$0.24 \pm 0.07$	$8.9 \pm 2.7$	0.46	$-106.9 \pm 0.9$	$10.2 \pm 0.9$
5	35	3	3	$2.52 \pm 0.17$	$3.71 \pm 0.55$	$6.35 \pm 0.03$	$0.23 \pm 0.06$	$7.4 \pm 2.1$	0.53	$-124.5 \pm 1.4$	$9.1 \pm 1.0$
5	40	0	3	$2.56 \pm 0.17$	$3.68 \pm 0.32$	$6.36 \pm 0.02$	$0.27 \pm 0.05$	$5.9 \pm 1.8$	0.55	$-140.8 \pm 1.6$	$8.0 \pm 1.2$
5	50	0	0	$2.67 \pm 0.18$	$3.59 \pm 0.17$	$6.35 \pm 0.02$	$0.27 \pm 0.04$	$6.0 \pm 1.1$	0.64	$-175.4 \pm 2.0$	$13.9 \pm 1.9$
10	30	21	1	$2.51 \pm 0.18$	$3.96 \pm 0.76$	$6.38 \pm 0.03$	$0.25 \pm 0.07$	$13.5 \pm 2.6$	0.45	$-107.2 \pm 1.2$	$14.2 \pm 0.8$
10	35	4	0	$2.52 \pm 0.17$	$3.70 \pm 0.53$	$6.35 \pm 0.03$	$0.23 \pm 0.06$	$11.4 \pm 1.9$	0.53	$-123.2 \pm 1.1$	$14.9 \pm 1.1$
10	40	0	0	$2.55 \pm 0.17$	$3.68 \pm 0.33$	$6.36 \pm 0.02$	$0.26 \pm 0.05$	$10.6 \pm 1.7$	0.54	$-141.3 \pm 1.5$	$15.6 \pm 1.4$
10	50	0	0	$2.67 \pm 0.17$	$3.59 \pm 0.17$	$6.35 \pm 0.02$	$0.28 \pm 0.04$	$10.8 \pm 1.1$	0.66	$-175.8 \pm 2.1$	$23.0 \pm 1.7$
20	30	18	0	$2.52 \pm 0.18$	$3.90 \pm 0.77$	$6.38 \pm 0.03$	$0.23 \pm 0.07$	$23.2 \pm 2.6$	0.47	$-106.7 \pm 1.1$	$22.1 \pm 0.8$
20	35	1	0	$2.52 \pm 0.17$	$3.66 \pm 0.54$	$6.35 \pm 0.03$	$0.23 \pm 0.06$	$20.6 \pm 1.9$	0.53	$-124.7 \pm 1.4$	$25.3 \pm 1.4$
20	40	0	0	$2.56 \pm 0.17$	$3.63 \pm 0.32$	$6.36 \pm 0.03$	$0.27 \pm 0.05$	$20.4 \pm 1.8$	0.55	$-141.3 \pm 1.7$	$26.9 \pm 1.6$
20	50	0	0	$2.67 \pm 0.17$	$3.59 \pm 0.17$	$6.35 \pm 0.02$	$0.27 \pm 0.04$	$20.8 \pm 1.0$	0.65	$-175.0 \pm 1.7$	$37.0 \pm 1.4$

**Table 5.** Same as Table 4 for  $\sigma_n = 5 \text{ m s}^{-1}$ .

$K_p$ ( $\text{m s}^{-1}$ )	$N$	$\tau_c$ (per cent)	$\tau_b$ (per cent)	$\ln \theta_1$ ( $\ln \text{m s}^{-1}$ )	$\ln \theta_2$ ( $\ln \text{d}$ )	$\theta_3$ ( $\text{d}$ )	$\theta_4$	$K_m$ ( $\text{m s}^{-1}$ )	rms ( $\text{m s}^{-1}$ )	$\ln \mathcal{L}_{\text{max}}$	$\ln \text{BF}$
5	30	33	1	$2.52 \pm 0.21$	$3.76 \pm 0.95$	$6.37 \pm 0.03$	$0.25 \pm 0.09$	$10.0 \pm 3.0$	2.27	$-109.7 \pm 2.3$	$8.5 \pm 1.4$
5	35	9	1	$2.50 \pm 0.20$	$3.85 \pm 0.81$	$6.36 \pm 0.03$	$0.23 \pm 0.08$	$8.5 \pm 2.5$	2.49	$-128.2 \pm 2.1$	$8.4 \pm 1.5$
5	40	1	8	$2.56 \pm 0.19$	$3.75 \pm 0.50$	$6.36 \pm 0.03$	$0.25 \pm 0.06$	$7.1 \pm 2.6$	2.53	$-147.5 \pm 2.6$	$7.1 \pm 1.4$
5	50	1	0	$2.60 \pm 0.18$	$3.68 \pm 0.29$	$6.36 \pm 0.02$	$0.25 \pm 0.06$	$6.3 \pm 1.6$	2.73	$-184.7 \pm 2.7$	$10.8 \pm 2.2$
10	30	28	0	$2.55 \pm 0.21$	$3.88 \pm 0.90$	$6.37 \pm 0.03$	$0.25 \pm 0.08$	$14.0 \pm 3.0$	2.32	$-110.1 \pm 2.0$	$12.3 \pm 1.4$
10	35	10	0	$2.52 \pm 0.20$	$3.90 \pm 0.88$	$6.36 \pm 0.03$	$0.23 \pm 0.08$	$12.1 \pm 2.6$	2.50	$-128.6 \pm 2.5$	$13.1 \pm 1.9$
10	40	3	0	$2.58 \pm 0.19$	$3.83 \pm 0.54$	$6.36 \pm 0.03$	$0.25 \pm 0.06$	$11.3 \pm 2.5$	2.55	$-147.9 \pm 1.9$	$12.6 \pm 1.6$
10	50	0	0	$2.62 \pm 0.18$	$3.66 \pm 0.30$	$6.36 \pm 0.02$	$0.24 \pm 0.05$	$11.6 \pm 1.6$	2.69	$-185.5 \pm 2.4$	$18.7 \pm 2.0$
20	30	25	0	$2.49 \pm 0.22$	$3.85 \pm 1.02$	$6.37 \pm 0.03$	$0.24 \pm 0.09$	$24.0 \pm 2.8$	2.32	$-108.8 \pm 2.2$	$19.1 \pm 2.0$
20	35	4	0	$2.54 \pm 0.20$	$3.84 \pm 0.90$	$6.35 \pm 0.03$	$0.23 \pm 0.08$	$22.2 \pm 2.6$	2.47	$-127.6 \pm 2.1$	$21.9 \pm 2.1$
20	40	0	0	$2.55 \pm 0.19$	$3.83 \pm 0.53$	$6.37 \pm 0.03$	$0.25 \pm 0.06$	$20.8 \pm 2.4$	2.51	$-147.4 \pm 2.0$	$23.4 \pm 2.1$
20	50	0	0	$2.61 \pm 0.18$	$3.63 \pm 0.29$	$6.36 \pm 0.02$	$0.24 \pm 0.05$	$21.3 \pm 1.6$	2.69	$-184.9 \pm 2.7$	$30.2 \pm 2.4$

between planet and stellar activity parameters when computing the error bars. This process results in increasing the error bars on  $K_m$  by typically a few per cent.

The quality of the planet detection within the RV time series is assessed using the so-called Bayes factor ( $B_F$ , see equation 2 from Díaz et al. 2014, for a proper definition) to compare the marginal likelihoods of models assuming 0 (i.e. stellar activity and white noise only) and 1 planet signature in the data sets. The resulting  $B_F$ , computed using the method introduced in Chib & Jeliazkov (2001), allows to derive the posterior odds ratio which gives an estimation of the significance of the retrieved planet signal in each data set. Following Jeffreys (1961), we take  $B_F > 150$  (5 in log) to be the criterion to diagnose a fair detection of K2-33b.

### 3.2 Results

We independently model the mock RV time series described in Section 2.3 using the process described in Section 3.1 and reject those for which (i) the MCMC process did not converge (e.g. posterior density presenting multiple local minima or stuck on one of the prior boundaries) or (ii)  $B_F$  lies below the planet detection threshold.

The outcomes for each value of  $N$  and  $K_p$ , averaged over all the 8 sets of 10 RV time series, are given in Tables 4 and 5 for  $\sigma_n$  of 2 and  $5 \text{ m s}^{-1}$ , respectively. We note that respectively 18–24 per cent and 25–33 per cent of data sets with  $N = 30$  are rejected for the two cases of considered white noises, mainly due to the fact the MCMC process tends to minimize  $\theta_4$ , resulting in strongly overfitting the data. Moreover,  $K_m$  is strongly overestimated in the remaining RV time series, consistently with Damasso et al. (2019) for similar cases with too few observational constraints.  $B_F$  is also affected by this overestimation, as evidenced by its surprisingly high values, especially for the lowest  $K_p$  considered in this study. This shows that most data sets with  $N = 30$  are too sparse to provide a dense-enough coverage of the rotation cycle, leading to excess flexibility for the GP and resulting in erroneous estimates for  $K_m$ .

The reconstruction of the data sets is considerably improved for  $N \geq 35$ , as evidenced by (i) the good agreement between the statistical properties of the RV curve (see Table 2) and the output GP parameters and (ii) the more accurate retrieval of  $K_m$  (see also the illustration given in Fig. 3). The overestimation noted for  $K_m$  at  $N = 30$  strongly decreases at  $N = 35$  and is no longer significant at  $N \gtrsim 40$ . We find that planet signatures of  $K_p \gtrsim 10 \text{ m s}^{-1}$  are reliably recovered at precisions of  $5\sigma$  and  $4\sigma$  for  $\sigma_n$  of 2 and  $5 \text{ m s}^{-1}$ ,

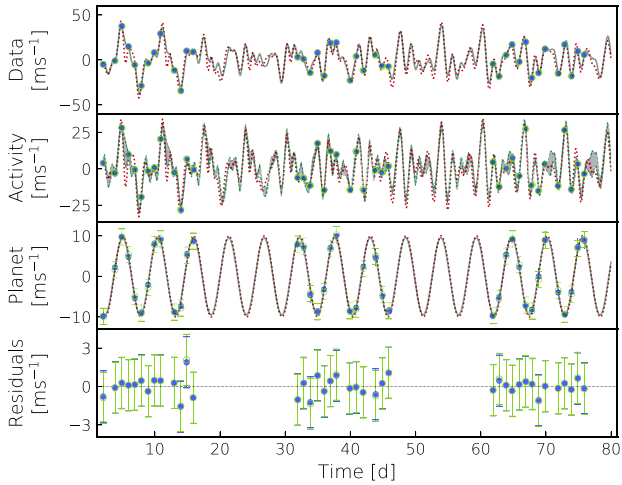


**Figure 3.** Best fit to one of our synthetic RV data sets containing  $N = 40$  data points and assuming  $K_p = 10 \text{ m s}^{-1}$  and  $\sigma_n = 2 \text{ m s}^{-1}$  rms. From top to bottom: RV data set, stellar activity RV signal, planet signature, and residuals. In each panel, the true RV signal is shown in red dotted lines, while the best predictions from the model are shown in green dashed lines and grey solid lines (resp.  $1\sigma$  error bands for panel 2), respectively, when imposing the orbital phase of the planet RV signal to be that derived from the photometry and when regarding it as a free parameter. Curves and data points in the two middle panels are obtained by subtracting from the synthetic data all the modelled components except that displayed in the panel.

respectively. Finally,  $K_p = 5 \text{ m s}^{-1}$  is fairly detected at  $3\sigma$  for  $N = 50$  data points while it remains marginally recovered for lower number of visits.

Imposing the planet orbital phase to be that derived from photometry barely improves the precision of  $K_m$  and does not significantly impact the detectability of the planet. Moreover, we find that low-to-moderate elliptical planet signatures with eccentricities  $\lesssim 0.2$  marginally impacts  $K_m$  as well as its error bars. We thus expect our algorithm to yield accurate estimates of the mass of K2-33b whose orbit is unlikely to be strongly elliptical (see Mann et al. 2016). Constraining the eccentricity of moderately elliptical planet orbits will require significantly more measurements than what we propose in this study, as assessed by preliminary simulations showing that uncertainties of the order of 0.15 on the eccentricity of the planet orbit require typically 100 visits to be achieved.

Finally, as already discussed in K19, in the specific case where the amplitude of the stellar activity signal is significantly larger than  $\sigma_n$  and the RV time series contain a low number of data points, the GP tends to adapt by slightly adjusting  $\theta_b$  to partly reconstruct the noise. Note that this trend decreases when  $\sigma_n$  and/or  $N$  increase in our simulations (see Tables 4 and 5).

#### 4 CONCLUSIONS

In this work, we simulated mass measurements of the young planet K2-33b, using synthetic RV time series assuming different sampling schemes, levels of white noise and semi-amplitudes of the planet signal. We found that 35/50 SPIRou visits spread on a 3-month visibility window are enough to reliably detect planet signatures of  $10/5 \text{ m s}^{-1}$  at precisions  $>3\sigma$  at a white noise level  $\lesssim 5 \text{ m s}^{-1}$ . Conversely, 30 visits over the same time span often yield synthetic data sets that can be inconclusive about the presence of the planet or lead to large errors in the estimated mass.

As suggested in M16, the substantial decrease in the stellar activity RV signal from visible wavelengths to the nIR makes K2-33 ideally suited for RV observations with high-precision nIR velocimeters like SPIRou. Our simulations demonstrate that the RV signature of the close-in Neptune-like planet K2-33b can be detected at a  $3\sigma$  level for a planet mass of  $\gtrsim 0.5 M_{\oplus}$ , provided that the observational sampling is dense enough.

K2-33b being significantly younger than all the planets with well-measured masses and radii, its nature is still unclear. Measuring the planet mass and hence probing its inner structure and composition will help unveiling its nature as well as constraining the evolution of its bulk density throughout the formation stage (see the review from Baruteau et al. 2016).

Consistently with K19, this study demonstrates the crucial need for RV follow-ups of stars hosting transiting planets to densely cover both the planet orbital period and stellar rotation cycles, on time-scales that are of the same order of the one on which stellar activity changes. Stars with activity features evolving on time-scales of tens of days, and rotation periods of only a few days, are therefore the most suited targets for RV follow-ups with high-precision velocimeters, as the mass of their transiting companions can be accurately measured in a single  $\sim 90$ -d window. NIR RV observations with sampling schemes similar to that we propose, as those being currently carried out in the framework of the SPIRou Legacy Survey, are thus likely to provide soon reliable mass measurements of transiting PMS planets such as K2-33 and V1298 Tau (David et al. 2016, 2019a, b).

#### ACKNOWLEDGEMENTS

This project was funded by the European Research Council (ERC) under the H2020 research & innovation programme (grant agreements #740651 NewWorlds). The authors would like to thank the referee for valuable comments and suggestions which helped improving the manuscript.

#### REFERENCES

- Aigrain S., Pont F., Zucker S., 2012, *MNRAS*, 419, 3147  
 Alibert Y., Carron F., Fortier A., Pfyffer S., Benz W., Mordasini C., Swoboda D., 2013, *A&A*, 558, A109  
 Baruteau C., Bai X., Mordasini C., Mollière P., 2016, *Space Sci. Rev.*, 205, 77  
 Berdyugina S. V., 2005, *Living Rev. Sol. Phys.*, 2, 8  
 Bouvier J., Bertout C., 1989, *A&A*, 211, 99  
 Chib S., Jeliazkov I., 2001, *J. Am. Stat. Assoc.*, 96, 270  
 Claudi R. et al., 2017, *Eur. Phys. J. Plus*, 132, 364  
 Crockett C. J., Mahmud N. I., Prato L., Johns-Krull C. M., Jaffe D. T., Hartigan P. M., Beichman C. A., 2012, *ApJ*, 761, 164  
 Damasso M., Pinamonti M., Scandariato G., Sozzetti A., 2019, *MNRAS*, 489, 2555  
 David T. J. et al., 2016, *Nature*, 534, 658  
 David T. J. et al., 2019a, *AJ*, 158, 79  
 David T. J., Petigura E. A., Luger R., Foreman-Mackey D., Livingston J. H., Mamajek E. E., Hillenbrand L. A., 2019b, *ApJ*, 885, L12  
 Díaz R. F., Almenara J. M., Santerne A., Moutou C., Lethuillier A., Deleuil M., 2014, *MNRAS*, 441, 983  
 Donati J. F. et al., 2016, *Nature*, 534, 662  
 Donati J.-F. et al., 2018, SPIRou: A NIR Spectropolarimeter/High-Precision Velocimeter for the CFHT. Springer Nature, Switzerland AG, p. 107  
 Foreman-Mackey D., Hogg D. W., Lang D., Goodman J., 2013, *PASP*, 125, 306  
 Haywood R. D. et al., 2014, *MNRAS*, 443, 2517

- Hébrard É. M., Donati J. F., Delfosse X., Morin J., Boisse I., Moutou C., Hébrard G., 2014, *MNRAS*, 443, 2599
- Howell S. B. et al., 2014, *PASP*, 126, 398
- Jeffreys H., 1961, *Theory of Probability*, 3rd edn. Oxford Univ. Press, Oxford
- Johns-Krull C. M. et al., 2016, *ApJ*, 826, 206
- Klein B., Donati J. F., 2019, *MNRAS*, 488, 5114
- Luger R., Agol E., Kruse E., Barnes R., Becker A., Foreman-Mackey D., Deming D., 2016, *AJ*, 152, 100
- Luger R., Kruse E., Foreman-Mackey D., Agol E., Saunders N., 2018, *AJ*, 156, 99
- Mahmud N. I., Crockett C. J., Johns-Krull C. M., Prato L., Hartigan P. M., Jaffe D. T., Beichman C. A., 2011, *ApJ*, 736, 123
- Mann A. W. et al., 2016, *AJ*, 152, 61
- Mordasini C., Alibert Y., Georgy C., Dittkrist K. M., Klahr H., Henning T., 2012, *A&A*, 547, A112
- Quirrenbach A. et al., 2014, in Ramsay S. K., McLean I. S., Takami H., eds, *Proc. SPIE Conf. Ser. Vol. 9147, Ground-based and Airborne Instrumentation for Astronomy V*. SPIE, Bellingham, p. 91471F
- Rasmussen C. E., Williams C. K. I., 2006, *Gaussian Processes for Machine Learning*. MIT Press, Cambridge, USA
- Reiners A., Shulyak D., Anglada-Escudé G., Jeffers S. V., Morin J., Zechmeister M., Kochukhov O., Piskunov N., 2013, *A&A*, 552, A103
- Wildi F. et al., 2017, in Shaklan S., ed., *Proc. SPIE Conf. Ser. Vol. 10400, Techniques and Instrumentation for Detection of Exoplanets VII*. SPIE, Bellingham, p. 1040018
- Yu L. et al., 2017, *MNRAS*, 467, 1342

This paper has been typeset from a  $\text{\TeX}/\text{\LaTeX}$  file prepared by the author.